UNIVERSITY OF CALIFORNIA

SANTA CRUZ

AN INCLUSIVE SEARCH FOR THE DECAY OF A BOOSTED HIGGS BOSON IN THE $H \to b\bar{b}$ CHANNEL WITH THE ATLAS DETECTOR

A dissertation submitted in partial satisfaction of the

requirements for the degree of

DOCTOR OF PHILOSOPHY

in

PARTICLE PHYSICS

by

Jacob Martin Pasner

October 2019

The Dissertation of Jacob Martin Pasner is approved:

Professor Jason Nielsen, Chair

Professor Abraham Seiden

Professor Michael Hance

Dean Lori Kletzer
Vice Provost and Dean of Graduate Studies

Table of Contents

List of Figures

List of Tables

Abstract

An Inclusive Search for the decay of a Boosted Higgs boson in the $H \to b\bar{b}$ channel with the ATLAS detector

by

Jacob Martin Pasner

Abstract placeholder

Dedication

Dedication

Dedication

Acknowledgments

Chapter 1

Introduction

Every dissertation should have an introduction. You might not realize it, but the introduction should introduce the concepts, backgrouand, and goals of the dissertation.

Part I

Theoretical Motivations and the Standard Model

Chapter 2

The Standard Model and Beyond

2.1 The Standard Model

The pinnacle of humanities ability to represent the fundamental fields and particles that build the universe, the Standard Model is the guiding theoretical basis of particle physics.

2.2 Quantum Chromodynamics

Quantum chromodynamics is super wack

2.3 Quandum Electrodynamics

Quantum Electrodynamics is the first model created in the QFT image.

2.4 Spontaneous Symmetry Breaking

Spontaneous symmetry breaking occurs when a system loses an inherent symmetry in order to attain a lower energy configuration.

2.5 The Higgs Mechanism

The Higgs Mechanism is the system by which particles attain mass through the spontaneous breaking of the Higgs potential, thus causing all particles it interacts with to have mass.

2.6 Parton Distribution Function

Before QFT the proton was thought to be a hard ball containing no smaller constituents. However, we know now that that the strong field inside the proton allows for any strong object to exist with some probability which changes based off of the total energy of the proton. This behavior is represented then by a Probability Distribution Function.

Part II

Experimental Apparatus and Associated Facilities

Chapter 3

The Large Hadron Collider

Located 100 meters under the Swiss / French boarder lies the 26.7 kilometer Large Hadron Collider (LHC) [1]. The culmination of a huge international collaboration, this apparatus is used to produce proton and heavy ion collisions for observation by the four major experiments at the LHC: ATLAS, CMS, LHCb, and ALICE. The system was designed for a maximum center-of-mass energy of $\sqrt{s} = 14$ TeV and a peak instantaneous luminosity of $L = 10^{34}\text{cm}^{-2}\text{s}^{-1}$.

The first LHC workshop was held in 1984 in Lausanne at the European Organization for Nuclear Reserach (CERN) [2]. The nearly 30 year old case for a machine that would push towards the discovery of the elusive Higgs Boson was presented using the existing CERN accerlerator facilities and the Large Electron Positron (LEP) collider tunnel. The proposal became reality on September 10, 2008 when the first proton beams were circulated, only to have calamity strike 9 days later in the form of a catastrophic electrical fault. The repairs and improvements lasted until November 2009 when the LHC restarted. Since then this modern marvel has worked wonderfuly and, as hoped, lead to the discovery of the Higgs Boson by the CMS and ATLAS collaborations July 4, 2013.

The following chapter provides a brief introduction to the worlds most powerful accelerator starting with the little red bottle of hydrogen in building XXX, and ending with the interaction point where protons collide at the highest energies ever produced.

3.1 Particle Incjecton Chain

We begin with the most common element in the Universe, hydrogen, as our source of protons. A bottle of hydrogen gas provides 100 microsecond pulses of raw H_2 which is then injected into a Duoplasmatron. There, a strong electric field and free elctrons from a cathode ionize the molecule into bare H^+ aka a proton! These protons are then accelerated by a 90kV field, leaving the Duoplasmatron with 1.4% speed of light (~4000km/s) or, in relativistic units, about 83KeV. The bare protons are then fed into the accelerating RadioFrequency (RF) cavities of Linear Accelerator 2 (LINAC2). Inside, conductors charged by a powerful oscillating electromagnetic field accelerate the protons resulting in a 50MeV energy. Along the way, small quadrupole magnets shape the proton packet insuring they remain in a tight beam. This pattern of accleration with RF cavities and shaping/turnig with magnets is then repeated with CERN's first

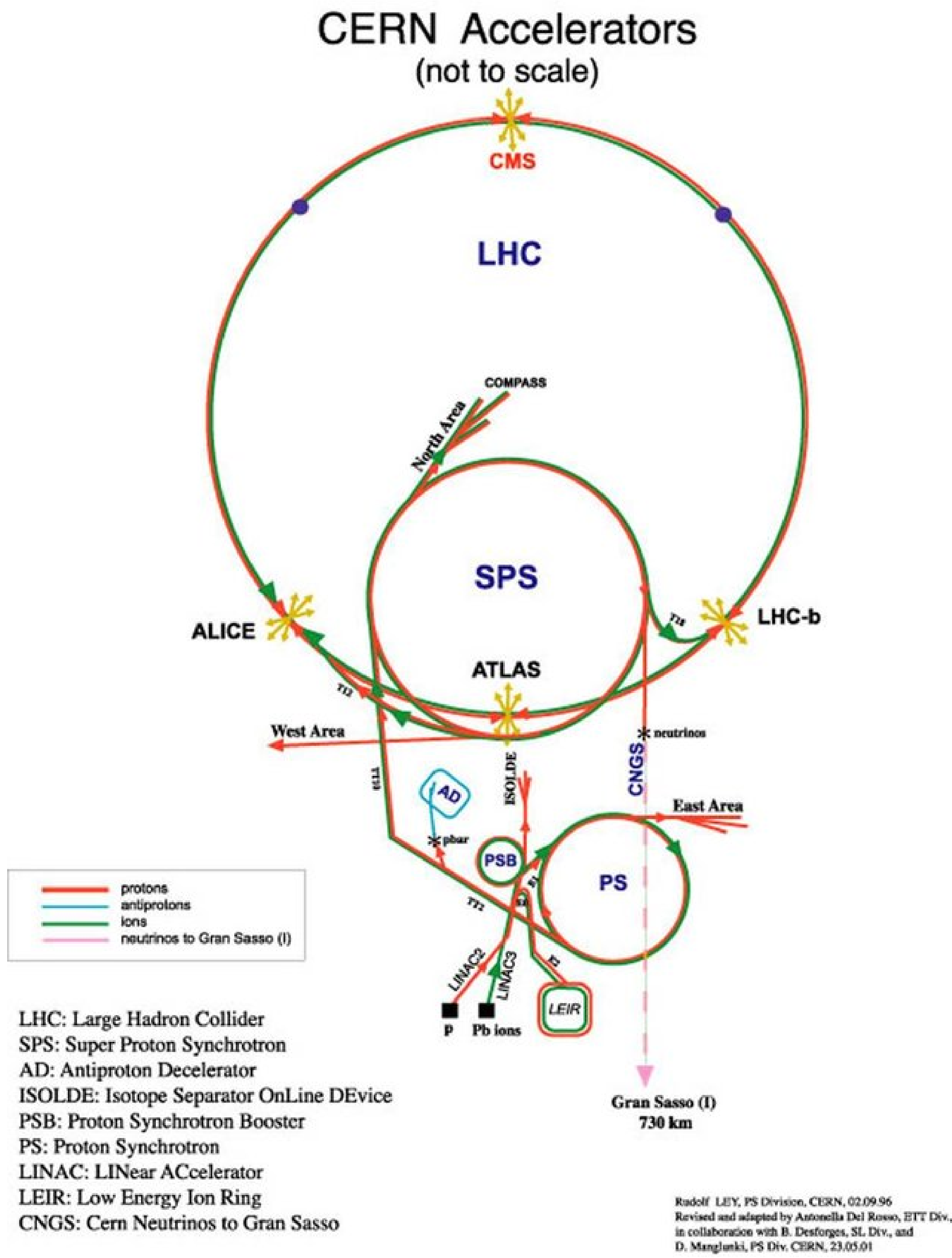

Figure 3.1: CERN accelerator complex

synchrotron, the Proton Synchrotron (PS) rendering a 1.4 GeV beam. The final step before the LHC comes with the Super Proton Synchrotron where the same technologies are implemented to produce 450 GeV protons, ready for injection into the LHC. A diagramatic representation of this chain can be seen in figure 3.1

In order to produce proton-proton collisions the LHC uses two beams circulating in opposite directions. The beams are not continuous, but instead consist of bunches, or buckets, of $\mathcal{O}(10^{11})$ protons with a spacing of 25ns. Given the LHC circumference this allows for 3564 buckets, however only 2808 are filled per beam due to safety requirements and injection limitations. Each beam takes 4 minutes and 20 seconds to fill and then an additional 20 minutes to for the protons to reach their maximum energy of 7 TeV TeV, or 99.99999991% the speed of light! Under normal operating conditions these beams can be used for many hours.

3.2 LHC layout and design

While often depicted as a perfect circle the LHC is in reality an octagon with rounded edges, called arcs, as can be seen in figure 3.2. Here you can see the counter circulating beams of protons depicted in red and blue. These beams are focused and collided at the 4 dedicated interaction points at rates of up to 40 MHz. Two of these points are occupoied by the ATLAS and CMS experiments, both of which are high luminosity, multi-purposed experiments.

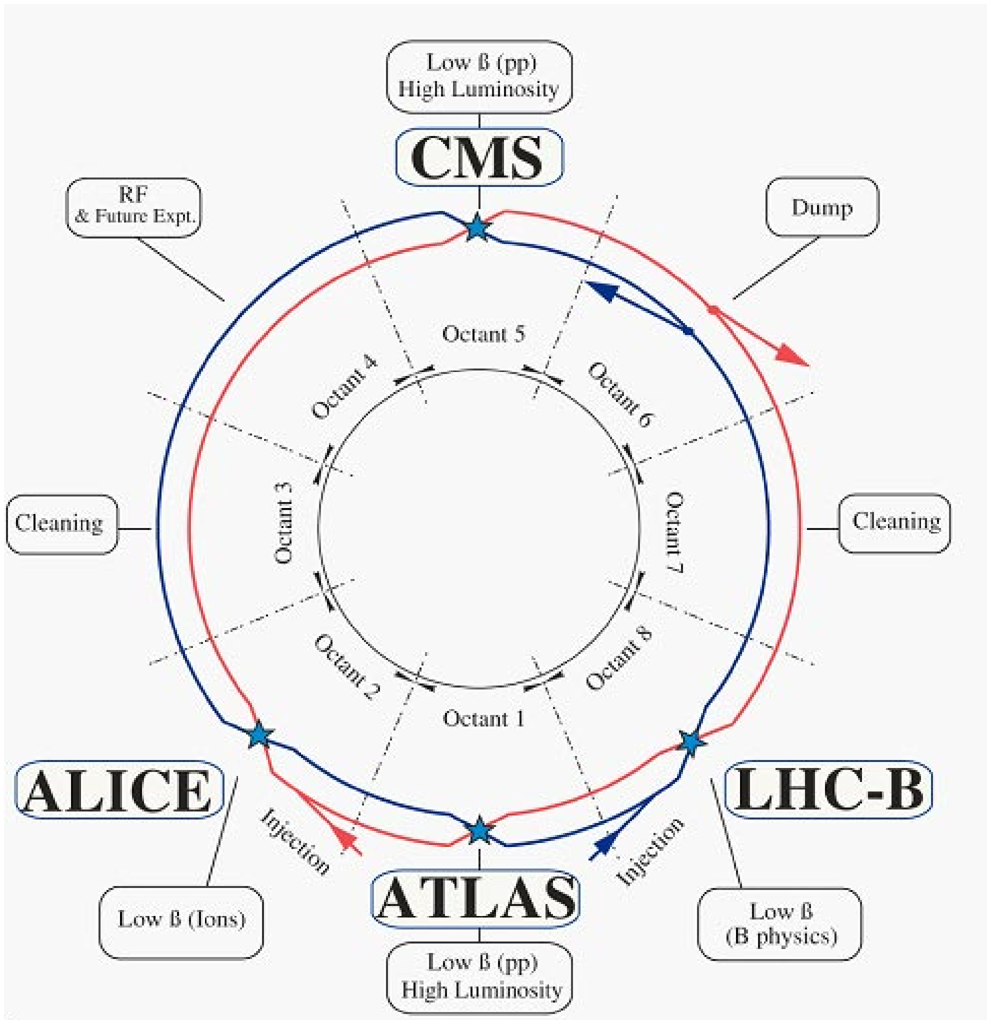

Figure 3.2: Labeled diagram of all the experiments at the LHC indicating the counter circulating beams and points of interest along the circumference of the accelerator.

The exact design of the tunnel is due to the experimental constraints of the original machine for which it was built, the Large Electron Positron (LEP) Collider. For the $\sim 2,000$ times lighter electron the maximum energy was limited by the synchrotron radiation, proportional to $\frac{1}{m^4}$, requiring long straight sections of accelerating RF cavities to recouperate the lost energy. Given that this effect is $\mathcal{O}(10^{13})$ times smaller for the proton the LHC is instead limited by our ability to design and construct magnets strong enough to bend the beam given the already determined curvature of the 8 arcs.

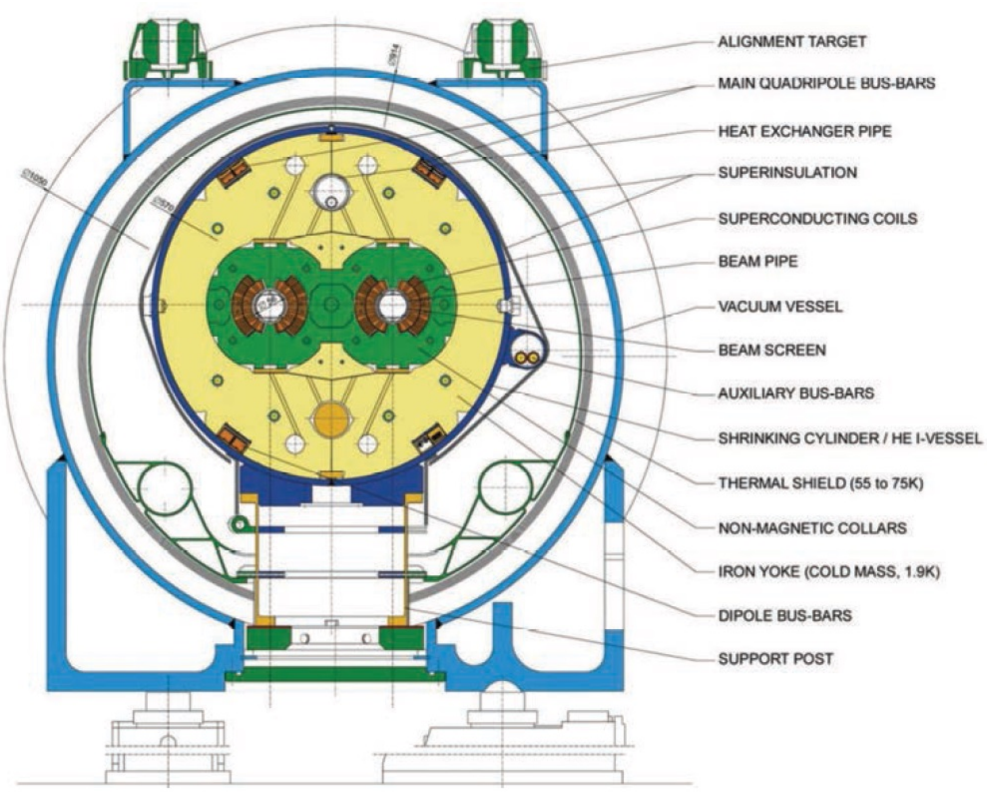

Figure 3.3: Depiction of a LHC dipole magnet 2-in-1 design labeling the major components

The oppositely circulating beams must each have their own ring and magnetic field which lead to the creation of a twin-bore (i.e. ”two-in-one”) magnet design, a cross section of which can be seen in figure 3.3. These magnets are constructed using NbTi superconductors which are cooled to 2K using superfluid helium. These magnets are designed to provide the needed 8.33 T magnetic field required to bend the beams at the design beam energy of 7 TeV. In total 1231 of these 15 m long bending dipole magnets are used, in association with 392 5-7m long quadrupole magnets which are responsible for keeping the proton bunches in a tight beam by squeezing them either horizontally or vertically.

3.3 Performance

Since the begining of its stable running in 2010 the LHC has performed well, even exceeding our expectations. While the experiment itself is incredibly complex, the performance of the machine, for the purposes of our analysis, can be reduced to two numbers; the familiar center of mass energy of the beams and a less common quantity known as the integrated luminosity.

For particle physics the integrated luminosity is proportional to the total number of collisions recorded during a specified time period, while the instantaneous luminosity is proportional to the bunch crossing rate along with the cross section of a proton-proton interaction and represents the potential number of collisions per second. Knowing this we can see that the integrated luminosity, L_{int} is simply the integral of the instantaneous luminosity $L_{inst.}$ for a choosen data period as seen in equation 3.1.

$$L_{int} = \int L_{inst.} dt \tag{3.1}$$

For a standard Gaussian beam, $L_{inst.}$ can be written as

$$L = \frac{N_b^2 n_b f_{rev} \gamma_r}{4\pi \epsilon_n \beta^*} F \tag{3.2}$$

where N_b is the number of particles per bunch, n_b the number of bunches per beam, f_{rev} the revolution frequency, γ_r the relativistic gamma factor, ϵ_n the normalized transverse beam emittance, β^* the beta function at the collision point, and F the geometric luminosity reduction factor due to the crossing angle at the interaction point given by

$$F = \left(1 + \left(\frac{\theta_c \sigma_z}{2\sigma^*}\right)^2\right)^{-1/2} \tag{3.3}$$

where θ_c is the full crossing angle at the interaction point, σ_z is the RMS bunch length, and σ^* is the transverse RMS beam size at the interaction point.

For the ATLAS experiment the integrated luminosity for each year can be seen in figure 3.4a as well as an example of the instantaneous luminosity for the choosen year in figure 3.4b.

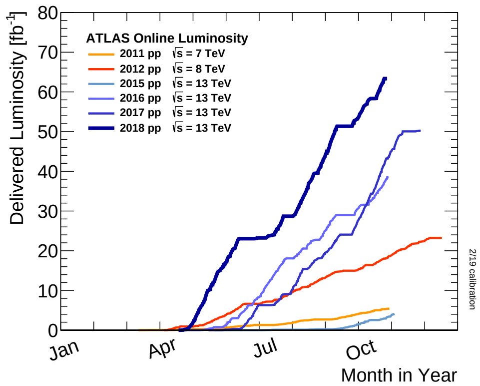

(a) Integrated Luminosity 2011 - 2018

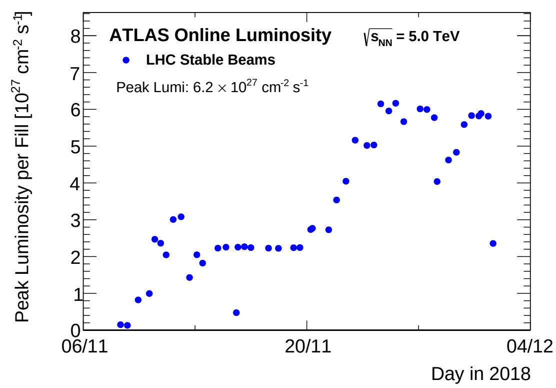

(b) 2018 Peak Instantaneous Luminosity

Figure 3.4: Luminosity is monitored as both a runing total known as the Integrated Luminosity as depicted in (a) and as an instantaneous quanity as shown in (b)

3.4 Pile-up at the LHC

Given the large number of protons per bunch and the cross-section of a proton-proton interaction, the probability to observe multiple interactions per bunch crossing is quite high. These multiple-interaction are known as pile-up, μ or the time averaged representation $\langle\mu\rangle$, and come in two different forms:

1. **In-time pile-up:** These are the other proton-proton collisions that occur during the same bunch crossing as the primary interaction that cauesd the Data Aquisition (DAQ) system to trigger. These are the standard extra interactions we expect to observe as stated above.

2. **Out-of-time pile-up:** These are interactions that occur either before or after a

bunch crossing that causes the DAQ to trigger. This effect is generally due to the long integration times of some detector electronics.

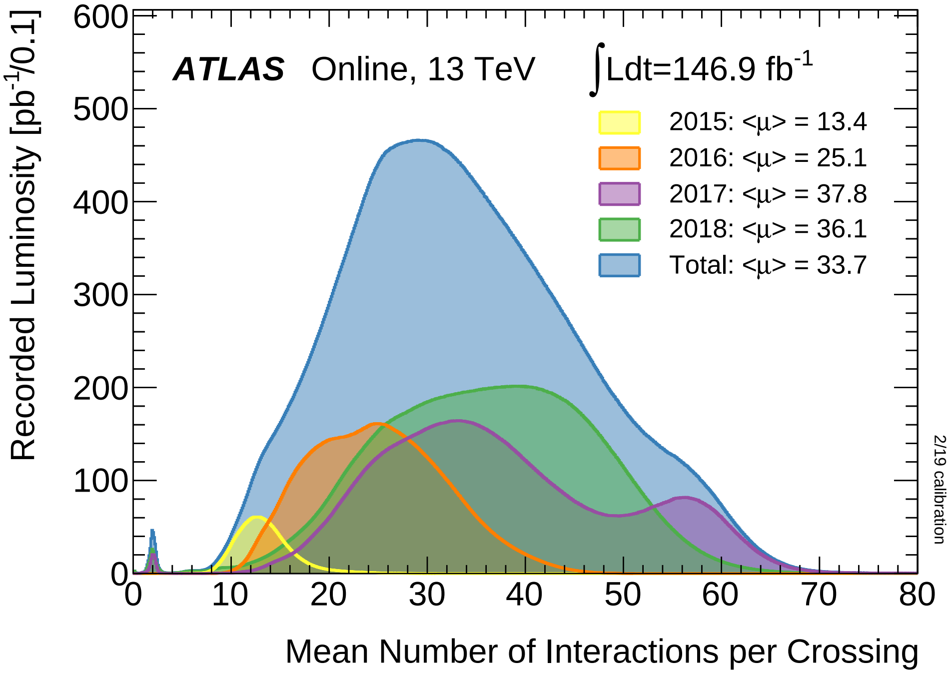

Figure 3.5: Pileup for data taking periods 2015 - 2018

The pile-up profile for past years can be seen in figure 3.5. The width of this distributino is due a combination of Poisonian statistics, the decrease in number of protons per bunch over the lifetime of a single run, and optimization tweaks to the beam's profile during runtime. Understanding and eliminating the noise from these pile-up events is crucial to reconstructing physics variables to represent the primary interaction we hope to observe.

Chapter 4

The ATLAS Detector

Given the immense energies availalbe at the LHC, and the veritable zoo of paricles we are trying to detect, we require a general-purpose experiment in order to fully exploit the full range of physics opportunities provided. Two international collaborations rose to this challenge, the CMS (Compact Muon Solenoid) and ATLAS (A Torroidal LHC ApparatuS) experiments. While both have similar physics goals and each of them strengths and weaknesses, this dissertation will focus on the ATLAS experiment and the intricacies of its three main sub-detectors and two massive magnet systems depicted in figure 4.1.

Originally proposed in 1994 the ATLAS experiment was completed in 2008. On July 4th, 2012 in a joint announcment the ATLAS and CMS experiments announced the discovery of the long predicted Higgs Boson. The collaboration now boasts over 3000 physicists from 175 instituations spread accross 38 countries and continues to probe

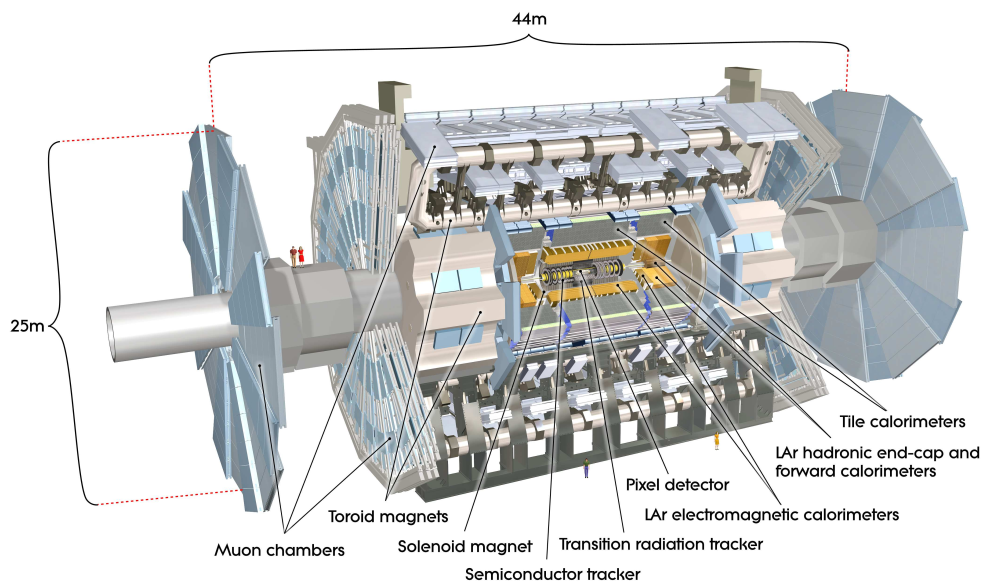

Figure 4.1: [3] Here we see a cut-away side view of the ATLAS detector with the major components labeled. Note that within each of these labeled components there may exist multiple different detector technologies. For scale two people in red are shown standing between the disk muon chambers on the left side of the figure.

the limits of the Standard Model in pursuit of answers to some of Humanities deepest questions.

Located approximately 100 meters underground in a vast excavated chamber, the ATLAS detector rests its 7000 metric tonnes on a bed of concrete reinforced steel. Out of it flows the signals of over 100 million electronic channels through a zip tied mass of greater than 3000 kilometers of cabling. At its very center is one of the four interaction points of the LHC, specifically Point 1, where the two counter circulating proton beams are skillfully shaped and then collided by a series of magnets. The energetic particles resultant from this collision then fly out in all directions into the bulk of the ATLAS detector.

The first sub-system they meet is the Inner Detector (ID) and its many layers of strip and pixel silcon detectors along with a transition radiation gaseous wire detector, all bathed in the 2T mangnetic field of the surronding superconducting solenoidal magnet. This system exploits the ionization of charged particles to track their curved trajectory through the magnetic field. This curvature gives us charge information, a momentum measurement, and precision 3D verticies crucial to the identification of the secondary verticies of a b-hadron decay.

Outside of the solenoid the particles are faced with first the Electromagnetic and then the Hadronic sampling calorimeters. Here, layers of scintillator and high radiation length materials are implemented to measure the energy of electrons, photons, and hadrons. As the goal is to completely absorb the energy of all outgoing particles the calorimeter has a nearly 4π solid angle coverage.

Finally we have the muon system surrounding the calorimeter and equipped with its own torroidal magnet system. Here the charged muon bends in the magnetic field while leaving a trail of ionization in the muon spectrometer before exiting the detector completely. Neutrinos are the only other standard model particle that leave the detector, however they do so without detection. A depiction of the various particle interactions with the different detector sub-systems can be seen in figure 4.2

In the following sections I will explain our choosen coordinate system and give a more detailed reveiw of these 3 detector sub-systems.

4.1 ATLAS Coordinate System

Using the nominal interaction point as the origin, ATLAS uses a right handed coordinate system where the positive x-axis points towards the center of the LHC ring, the positive y-axis points upwards, and the positive z-axis is defined by the counter clockwise circulating beam direction as viewed from above shown in figure 4.3 [3].

Using these coordinates we can define the physical momentum of the objects measured as $\vec{p} = (p_{\mathrm{T}}, p_z)$ with p_{T} being the momentum of the object in the transverse plane and p_z the momentum along the beam axis. Given the cylindrical symmetry of ATLAS it is desireable to define the polar angle θ from the beam axis with the $r - \phi$ plane being perpendicular to that axis. Since the particles we observe are relativistically boosted

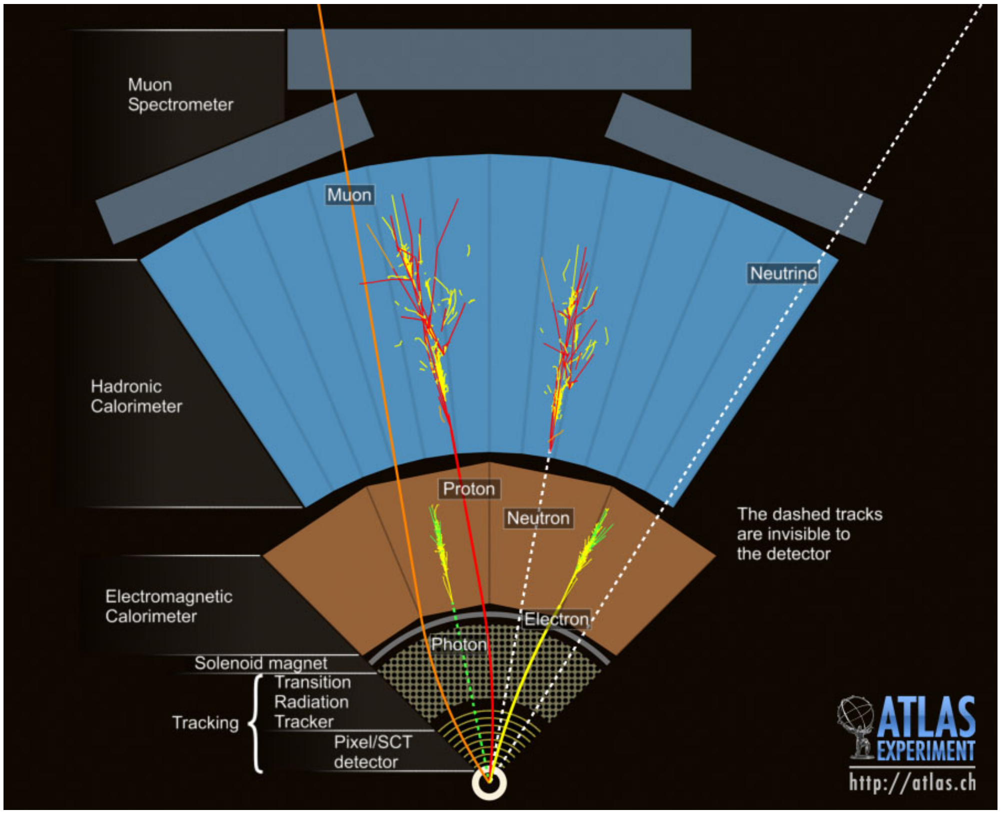

Figure 4.2: This slice of the ATLAS detector depicts how different particles interact with each component of the detector it crosses. A dashed line indicates no interaction while a solid line indicates interaction. Electrons (yellow/green) and charged hadrons (red) interact with the tracker and curve in the solenoid's magnetic field. Electrons and photons (yellow/green) are absorbed by the Electromagnetic calorimeter. All hadrons (red/yellow) are absorbed by the Hadronic calorimeter. The muons (orange) curve in both the solenoid and torroid magnetic fields before exiting the detector. Finally, the neutrinos (white) pass through the entire detector without interacting.

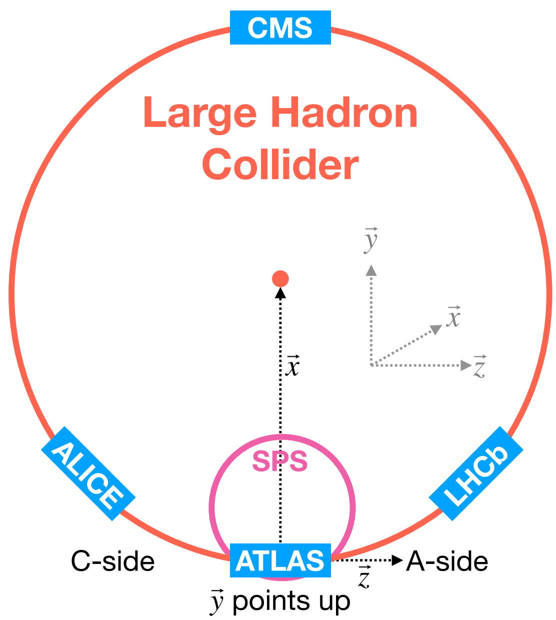

Figure 4.3: [4] A cartoon view of the the LHC from above showing the SPS, LHC and the four main experiments of the LHC: ATLAS, CMS, LHCb, and ALICE. The standard cartesian coordinate system is shown with its origin at the ATLAS interaction point, the positive x-axis towards the center of the LHC, the positive y-axis pointing upwards, and the positive z-axis pointing along the beamline towards the "A-side"

in the z-axis it is desireable to use the Lorentz invariant quantity pseudorapidity (η) defined in terms of the polar angle by

$$\eta = -\ln\tan\left(\frac{\theta}{2}\right). \tag{4.1}$$

where $\eta = 0$ is in the $x - y$ plane and larger values of $|\eta|$ being closer to the beam axis as can be seen in figure 4.4.

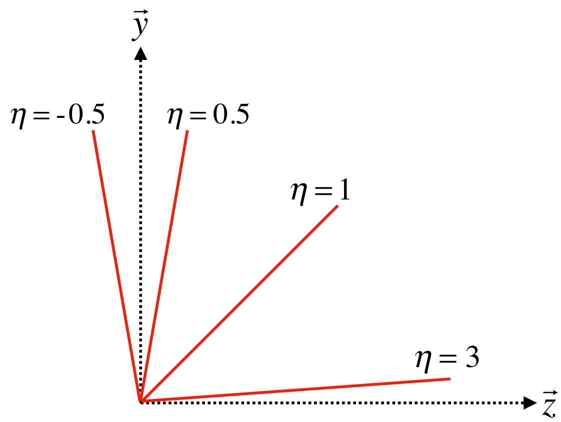

Figure 4.4: Modified from [4] this cartoon represents a selection of pseudorapiditity (η) values overlaid with some cartesian coordinates (dashed black lines). The redlines are drawn for $\eta = \pm 0.5, 1.0, 3.0$

In this analysis the angular separation between objects in the detector is calculated and represented using the geometric quantity

$$\Delta R = \sqrt{(\Delta\eta)^2 + (\Delta\phi)^2} \tag{4.2}$$

4.2 Tracking with the Inner Detector

With its closest component, the insertable b-layer (IBL) [5], only 3.3 cm from the interaction point The Inner Detector (ID), shown in figure 4.5 [6, 7], faces the incredible challenge of providing precision momentum resolution and identification of both primary and secondary vertex measurements of charged tracks all while recieving the highest fluence.

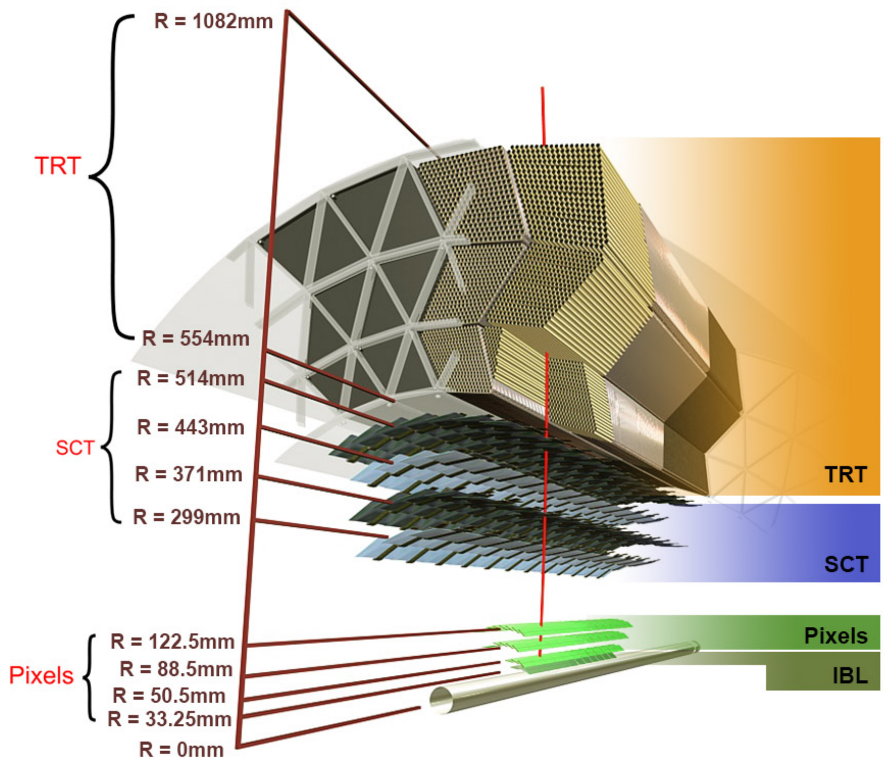

Figure 4.5: [5] Diagram of inner detector

It is designed to be very compact to reduce the probability of a particle decaying inside and to give precision measurements of the particles curvature in the 2T solenoidal magnetic field. This leades to excellent momentum resolution above the nominal p_{T} threshold of 0.5GeV and within the pseudorapidity range of $|\eta| < 2.5$ as shown in figure 4.6

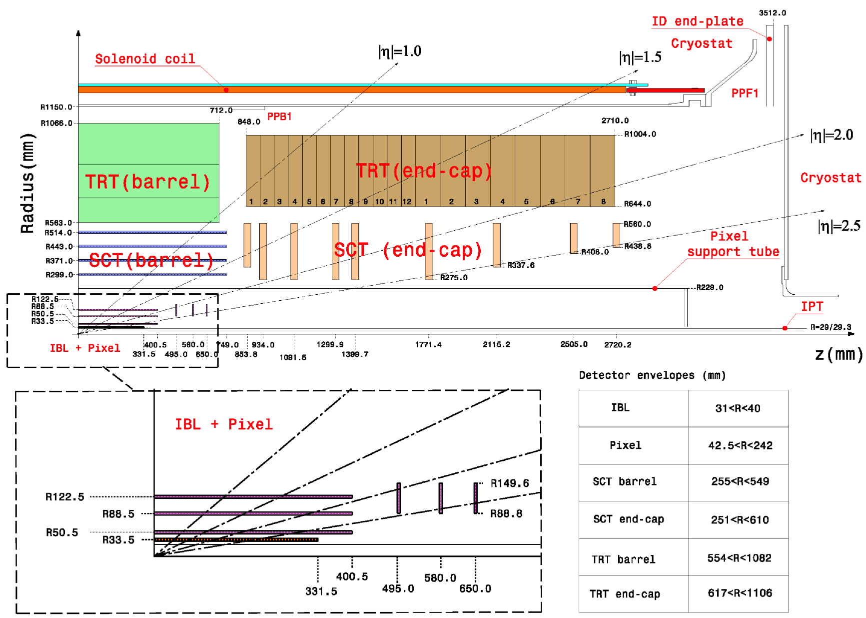

Figure 4.6: [8] Schematic of the Inner Detector including eta lines. Each component shown is cylindrically symmetric leading to a multi-layered detector.

The ID is composed of three different detector technologies for particle trajector reconstruction: The Pixel Detector, Semiconductor Tracker (SCT) and the Transition Radiation Tracker (TRT). These will be discussed in the following sections.

4.2.1 Pixel Detector

The ATLAS Pixel Detector [3], the innermost subdetector of the ID, is designed to give the best resolution possible as close as possible to the interaction point. This is accomplished using the 4 barrel layers and the 3 disks per endcap as indicated in figure 4.6. The inner most barrel layer, the IBL, has pixel dimensions of $50\mu\text{m}(\hat{\phi}) \times 250\mu\text{m}(\hat{z}) \times 200\mu\text{m}(\hat{r})$. For the other layers the dimensions are $50\mu\text{m}(\hat{\phi}) \times 400\mu\text{m}(\hat{z})$ for about 90% of the pixels and $50\mu\text{m}(\hat{\phi}) \times 600\mu\text{m}(\hat{z})$ for the others, all with a thickness of $250\mu\text{m}(\hat{r})$. This gives a total active area of 1.88m^2 collected through 92.4 million readout channels, more than half of the total number of channels for ATLAS. This detailed charged particle information very close to the interaction point is crucial not only for pattern recognition for track reconstruction, but also for the reconstruction of the primary and secondary verticies intrinsic to the decay of a b-hadrons, a critical element of the analysis presented in this thesis.

4.2.2 Semiconductor Tracker

Encompassing the Pixel Detector, the Semiconductor Tracker (SCT) [3] is composed of double sided silicon microstrips modules. Each side of the 4088 modules is constructed out of two silison strip sensors that are daisy chained togeather. The result is 768 composite strips each 12.6cm with an inter-strip pitch of $80\mu\text{m}$. In the barrel the strips are alligned with the $\hat{z}$ direction, while in the end caps they are aligned with the $\hat{r}$ direction. In both cases the separation of the strips is constant in $\hat{\phi}$. The two sides are rotated with respect to eachother by 40μm to allow for position measurement along the length of the strip. These modules are then used to tile the 4 barrel layers and 9 disks per endcap (18 disks in total) as seen in figure 4.6. This design is choosen to ensure that each charged track interacts with 8 strip layers (equivalent to four space points). This information is used to further measure the momentum and impact parameter, and as well as vertex identification of charged particles.

4.2.3 Transition Radiation Tracker

The Transition Radiation Tracker [3], the outermoust subdetector of the ID, provides tracking through the detection of transition radiation from ultra-relativistic charged particles for $\eta < 2.0$ using 350,000 drift tube channels also known as straws. The 4mm diameter straws are filled with a 70% Xe, 27% CO_2, and 3% O_2 gas mixture and a 31μm diameter gold-plated tungsten wire anode at the center for the collection of the ionization signal. In the barrel 73 azimuthally symetric layers of 144cm straws are oriented parallel to the beam pipe with an electrical division in the center of each allowing the two sides to be read out separately. For each endcap the straws are radially oriented in 160 symmetric planes each containing 768 37cm long drift tubes showin in figure 4.6. In both the barrel and the end caps polypropylene fibers (barrel) or foils (encaps) function as the transition radiation material which causes the relativistic charged particles to radiate and thus ionize the gas in the straw. The ammount of transition radiation produced is proportional to the Lorentz factor meaning that lighter particles (e.g. electrons) will produce more radiation. Thus, by defining a high and low threshold, we can identify tracks belonging to electrons by requiring they register more high-threshold hits. There are typically 36 TRT hits per charged track.

4.3 Calorimetry

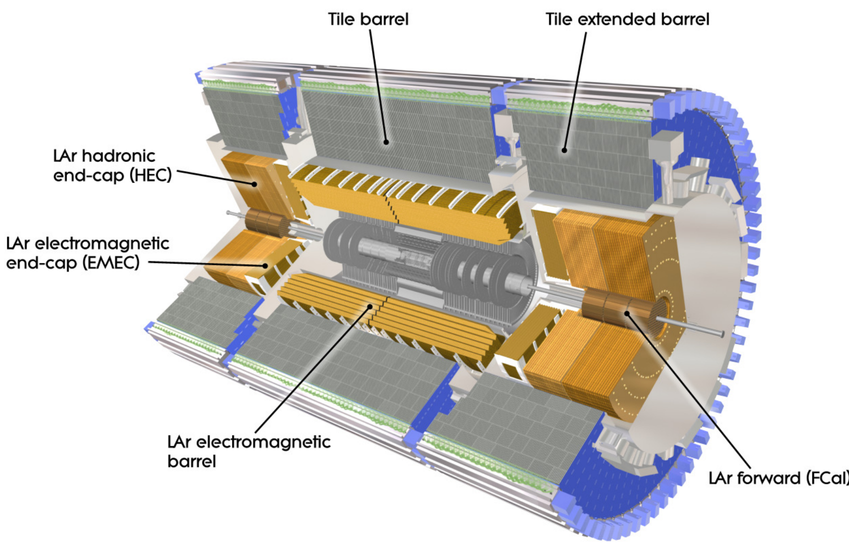

Figure 4.7: [3] A cutaway diagram of ATLAS's sampling calorimeters

Once the proton collision remnants have passed through the ID and it's surrounding solenoid they enter into the ATLAS calorimeters depicted in figure 4.7. Sampling calorimeter technologies were choosen for their compact geometry and lower cost point. These are constructed by alternating layers of absorber, a dense material which reduces the incedent particles energy, and active material which produces a detectible signal when a partilce passes through. This means that the detected signal is only a fraction of the total energy of the particle and thus requires a study of the calorimeter response for calibration purposes [9]. The first system, the Electromagnetic Calorimeter (EMC), is designed to measure the energy of electrons and photons which primarily lose their energy via bremstralung and pair production electromagnetic interactions. Outside of the EMC is the Hadronic Calorimeter (HC) which is designed to measure the energy of jets of hadrons through their electromagnetic and strong interactions. These detectors cover the entire $|\eta| < 4.9$ range and provide complete containment of both Electromagnetic and Hadronic showers with higher granularityi in the EMC for $|\eta| < 2.5$, the region matched to the ID, for precision measruements of electrons and photos. By instrumenting this huge space in $|\eta|$ we can search for events with asymetric energy deposits which imply the existence of a particle we didn't detect represented by missing transverse energy $E_{\mathrm{T}}^{\mathrm{miss}}$.

4.3.1 Electromagnetic Calorimeter

The innermost calorimeter, the Liquid Argon (LAr) Electromagnetic Calorimeter (EMC) [3], uses lead as the absorber and liquid argon as the active material in an "accordion geometry" as seen in figure 4.8. This geometry was choosen for uniform coverage in $\hat{\phi}$ due to its lack of un-instrumented cracks in the radial direction. The barrel region covers $|\eta| < 1.475$ and an end cap on each side covers $1.375 < |\eta| < 3.2$ each housed in their own cryostat. The barrel is composed of two half barrels with a 4mm gap at $z = 0$ and both end caps are divided into an intter wheel covering $2.5 < |\eta| < 3.2$ and an outer wheel covering $1.375 < |\eta| < 2.5$.

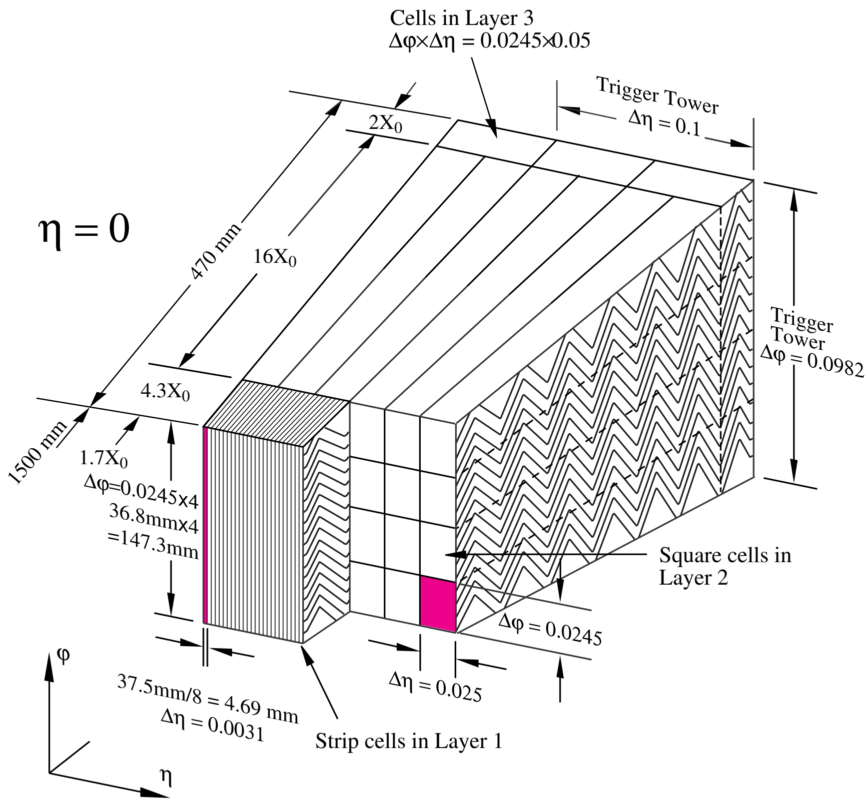

Figure 4.8: [3] Sketch of LAr EMC barrel module where the lead and liquid argon layers are visible in an accordion like geometry. Looking from the foreground to the back there are 3 different types of cells visible.

In the $|\eta| < 2.5$ region the EMC has 3 radial layers for precision physics measurements. Layer 1 consists of strip cells which are finely segmented with $\Delta\eta = 0.0031$ and $\Delta\phi = 0.0245$ allowing for precision position resolution which gives discrimination power between a single γ deposit and the π^0 characteristic $\gamma\gamma$ deposit. Layer 2 , which collects the largest fraction of energy from electromagnetic shower, is segmented with

$\Delta\eta = .025$ and $\Delta\phi = 0.0245$. Layer 3 collects the tail of the electromagnetic shower using a coarser segmentation of $\Delta\eta = .05$ and $\Delta\phi = 0.0245$. Additionally, in the region $|\eta| < 1.8$ a thin pre-sampler , which contains no lead absorber, was placed in front of Layer 1 to allow for energy corrections due to losses upstream of the EMC. Combined the EMC is > 22 radiation lengths (X_0) in the barrel and > 24 X_0 in the end-caps, where a radiation length is the average distance an electron travels in a given material before losing $1/e$ of its original energy E_0 via bremsstrahlung radiation.

4.3.2 Hadronic Calorimeter

Directly outside the EMC envelope is the Hadronic Calorimeter (HC) system [3] which consists of three sampling calorimeter technologies: the Tile calorimeter, the LAr hadronic end-cap calorimeter (HEC) and the LAr forward calorimeter (FCal). Combined, these three subsystems give measurements of hadronic jet energies in the $0 < |\eta| < 4.9$ range. The tile calorimeter uses steel as the absorber layer and scintillating tiles as the active material and covers the region $|\eta| < 1.7$ with a barrel section flanked by two barrel extensions each divided azimuthally into 64 modules. These scintillator tiles are read out on two sides by wave-length shifting fibers connected to photomultiplier tubes as seen in figure 4.9. At $\eta = 0$ the total tile calorimeter thickness is 9.7 nuclear interaction lengths (λ), where λ is the average distance a hadron travels before interacting inellastically with a nucleus.

The HEC is composed of two independent wheels per end-cap located just past the

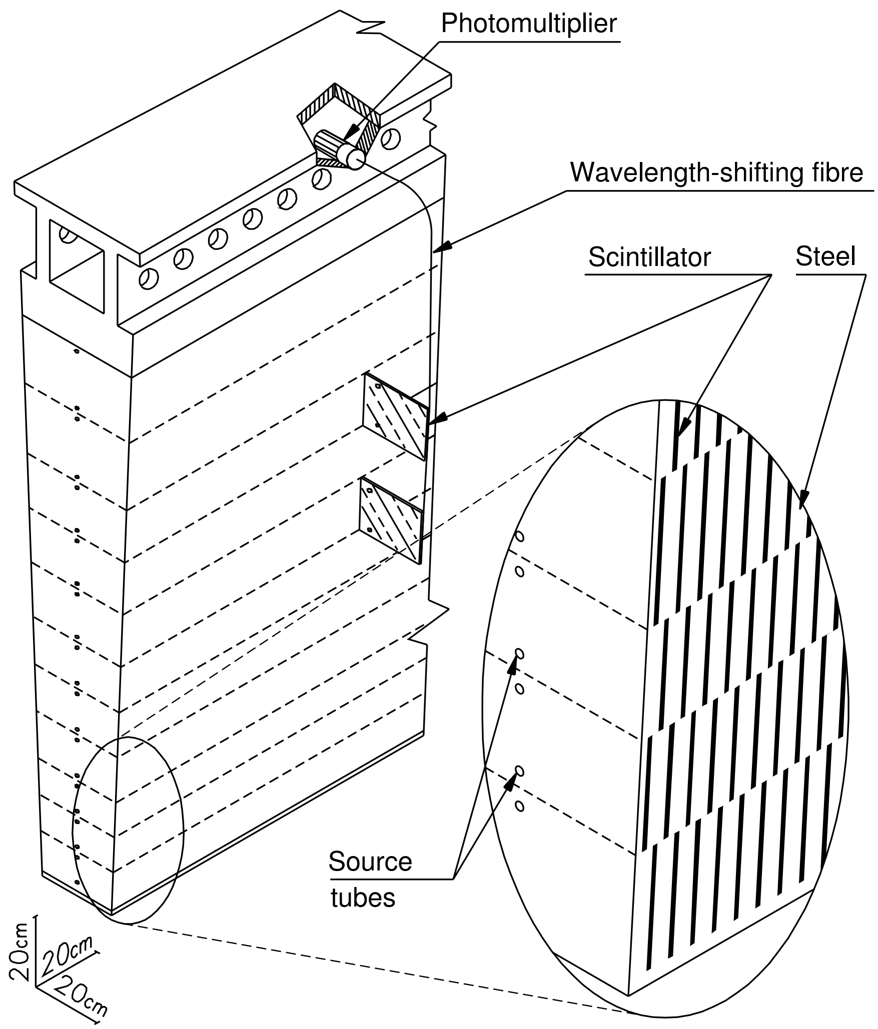

Figure 4.9: [3] Schematic of a tile calorimeter module including a depiction of the connection between the scintillator tile to the photomultiplier via a wavelength-shifting fibre.

EMC end-cap but sharing the same cryostat. This system uses copper as an absorber and liquid argon for the active material and covers the $1.5 < |\eta| < 3.2$ range using 32 wdge-shaped modules per wheel. Finally, the FCal shares the same cryostat as the EMC and HEC end-caps and acts to extend the coverage of the combined calorimeter system to include the $3.1 < |\eta| < 4.9$ range. Each endcap contains 3 modules, the first an electromagnetic module (Copper/Liquid-Argon) which is followed by two hadronic modules which use (Tungsten/Liquid-Argon.

4.4 Muon Spectrometer

The ATLAS Muon Spectrometer (MS) [3], see figure 4.10, accomplishes tracking of charged particles in the $|\eta| < 2.7$ region for momentum reconstruction while also providing triggering on charged particles in the $|\eta| < 2.4$ region. The magnetic field necessary for momentum reconstruction is provided by 3 air core torroid systems, one barrel torrioid covering $|\eta| < 1.4$ and two endcap torroid systems which are inserted into the inner radius of the the barrel torroid to cover the $1.6 < |\eta| < 2.7$. The so called transition region $1.4 < |\eta| < 1.6$ between these two magnet systems is covered by a combination of the barrel and endcap torroid magnets. Similar to the ID the resolution is inversely proportional to the particle's incident momentum. Any muon with pT lower than 3GeV will never make it to the MS and thus will not be detected.

Precision tracking measurements for momentum reconstruction is accomplished using

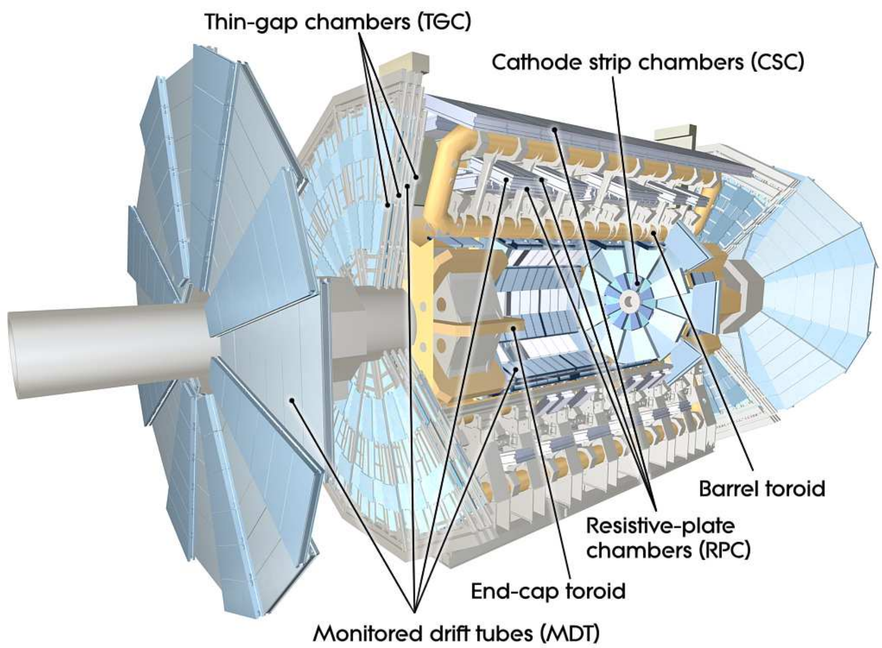

Figure 4.10: [3] A cut-away diagram of the ATLAS muon system and its many sub-detectors.

the Monitored Drift Tube chambers (MDTs) for $|\eta| < 2.0$ and using Cathode-Strip Chambers (CSCs) for $2.0 < |\eta| < 2.7$. The MDT system consists of 1163 drift tube chambers arranged in three to eight layers for varying η. The CSCs are designed to withstand the higher rate and retain good time resolution using multiwire proportional chambers with orthogonal segmented cathode planes.

The MS also gives nanosecond tracking information for triggering on muon tracks. This is accomplished using Resistive Plate Chambers (RPC) in the barrel region $|\eta| < 1.05$ and Thin Gap Chambers (TGC) in the end-cap $1.05 < |\eta| < 2.4$ region. Both chamber systems deliver a triggerable signal with a spread of $15-25$ ns, thus providing the ability to tag individual beam-crossings.

Chapter 5

Boosted Higgs at the LHC

Its July 4th, 2012 and the walls of building 500 are reverberating as Particle Physicists around the world rejoice the discovery of the particle that gives all things mass, the Higgs Boson.

5.1 Physics beyond the Stnadard Model

5.2 Higgs Production Mechanisms

5.3 Branching Ratios

5.4 Discovery

5.5 Fermion Decay Modes

5.6 Boosted Higgs

Part III

The HbbISR Analysis

Chapter 6

Data and Simulation Preparation

In order to compare data to theory ATLAS has developed an anlysis chain which runs both real data and simulated samples through the same processing, assuring a final result which is as comprable as possible.

6.1 Data Used

6.2 Monte Carlo Samples

Chapter 7

Physics Object Selection

After the ATHENA Digitization step both data and monte carlo have the same format, representing the three dimentional energy deposits. In order to analyze these deposits they are cleaned, clustered and checked for overlap resulting in physics objects useful for our specific analysis.

7.1 Calorimeter Jets

7.2 Track Jets

7.3 Fat Jets

7.4 B-tagged Jets

7.5 Muons

7.6 Overlap Removal

Chapter 8

Event Selection

Having created our physics objects we begin to make selections of what types of events we want to consider given the goal of our analysis. In our boosted topology this means considering things like momentum, jet collection efficiencies and background rejection.

8.1 Selected Triggers

8.2 Pre-selection Studies

8.3 Signal Selection

8.4 Optimisation

Chapter 9

Background Estimation

The dominant background was QCD. I worked on the ttbar control region. The Vqq and single top backgrounds were estimated from monte carlo.

9.1 Multi-jet QCD estimation

9.2 $t\bar{t}$ control region

9.3 Single top estimation

9.4 Hadronic vector boson channel

Chapter 10

Systematic Uncertanties

10.1 Theoretical Uncertanties

10.2 Experimental Uncertanties

Chapter 11

Statistical Fit

The statistical fit in our analysis was accomplished using a framework developed for Higgs searches.

11.1 Profile Likelihood Function

11.2 Fit Configruation

11.3 Statistical Tests

Chapter 12

Results

12.1 Expectations

12.2 Statistical Analysis Results

12.3 Measurements and Limits

Part IV

Conclusion

Chapter 13

Conclusion

I conclude that this secion is the conclusion

Bibliography

[1] Lyndon Evans and Philip Bryant. “LHC Machine”. In: *JINST* 3 (2008), S08001. DOI: `10.1088/1748-0221/3/08/S08001` (cit. on p. 6).

[2] Chris Llewellyn Smith. “Genesis of the Large Hadron Collider”. In: *Phil. Trans. Roy. Soc. Lond.* A373.2032 (2014), p. 20140037. DOI: `10.1098/rsta.2014.0037` (cit. on p. 6).

[3] ATLAS Collaboration. “The ATLAS Experiment at the CERN Large Hadron Collider”. In: *JINST* 3 (2008), S08003. DOI: `10.1088/1748-0221/3/08/S08003` (cit. on pp. 17, 19, 25–33).

[4] Giordon Holtsberg Stark. “The search for supersymmetry in hadronic final states using boosted object reconstruction”. Presented 26 Apr 2018. May 2018. URL: `https://cds.cern.ch/record/2317296` (cit. on pp. 21, 22).

[5] Karolos Potamianos. *The upgraded Pixel detector and the commissioning of the Inner Detector tracking of the ATLAS experiment for Run-2 at the Large Hadron Collider*. Tech. rep. ATL-PHYS-PROC-2016-104. 15 pages, EPS-HEP 2015 Proceed-

ings. Geneva: CERN, Aug. 2016. URL: https://cds.cern.ch/record/2209070 (cit. on p. 23).

[6] *ATLAS inner detector: Technical Design Report, 1*. Technical Design Report ATLAS. Geneva: CERN, 1997. URL: http://cds.cern.ch/record/331063 (cit. on p. 23).

[7] S Haywood et al. *ATLAS inner detector: Technical Design Report, 2*. Technical Design Report ATLAS. Geneva: CERN, 1997. URL: https://cds.cern.ch/record/331064 (cit. on p. 23).

[8] B. Abbott et al. "Production and integration of the ATLAS Insertable B-Layer". In: *JINST* 13 (2018), T05008. DOI: 10.1088/1748-0221/13/05/T05008. arXiv: 1803.00844 [physics.ins-det] (cit. on p. 24).

[9] Christian Wolfgang Fabjan and F Gianotti. "Calorimetry for Particle Physics". In: *Rev. Mod. Phys.* 75.CERN-EP-2003-075 (Oct. 2003), 1243–1286. 96 p. DOI: 10.1103/RevModPhys.75.1243. URL: https://cds.cern.ch/record/692252 (cit. on p. 28).

Appendix A

Hadronic Vqq Sherpa Studies

Ancillary material should be put in appendices, which appear after the bibliography.